npj | clean water

Article

Published in partnership with King Fahd University of Petroleum & Minerals

https://doi.org/10.1038/s41545-025-00489-9

Innovative dual-purpose remediation of acid mine drainage and resource recovery through membrane distillation crystallization

Lebea N. Nthunya[1] ✉, Aamer Ali[2], Heidi Richards[3], Luke Chimuka[3], Cejna Quist-Jensen[4] & Bhekie B. Mamba[1]

The current study evaluated the innovative application of membrane distillation crystallization (MDCr) for dual treatment and resource recovery from acid mine drainage (AMD), a persistent environmental crisis in South African. This AMD was characterized by exorbitant concentrations of Ca^{2+} (2622 mg·L^{-1}), Fe^{2+} (1421 mg·L^{-1}), SO_4^{2-} (9790 mg·L^{-1}) and Cl^- (1113 mg·L^{-1}). The current study evaluated the performance of hollow fibre polypropylene membrane in processing both acidic (pH 3.58) and neutralized (pH 6.47) feedwaters. The permeate was 3.3 kg·m^{-2}·h^{-1}, 2.2 kg·m^{-2}·h^{-1} and 1.3 kg·m^{-2}·h^{-1} at 70, 60 and 50 °C respectively, which remained relatively stable at high recovery factors (>80%). Acidic AMD promoted formation of large metal-rich ettringite and halite crystals while neutralized AMD produced small and dense ettringite, hexahydrite and jarosite crystals. This study highlighted the dual functionality of MDCr in water treatment and mineral resource recovery, offering a sustainable solution to address the AMD pollution crisis in South Africa.

Acid mine drainage (AMD) is one of the most concerning environmental challenges characterized by acidic water containing dissolved metals, sulphates, and trace elements[1]. The low pH of AMD, often aggravated by deposits of iron pyrite, facilitates the dissolution of hazardous metals[2]. Consequently, this renders AMD a threatening source of water pollution in various water bodies and surrounding ecosystems[3]. Due to a range of abandoned and closed mines, various countries with an extensive history of mining activities are faced with a legacy of AMD crisis[4]. This is no exception in South Africa, a country of various mining activities for the past 120 years[5]. This issue is further intensified by the semi-arid climate conditions heightening water scarcity, resultantly amplifying the socio-economic impacts[6,7]. Based on South African National Water Act No. 36 of 1998 and Water Quality Guidelines (DWAF, 1996), the discharge of AMD is regulated based on the following conditions: pH (5.5–5.9), total dissolved solids (≤1000 mg·L^{-1}), sulphate (≤250 mg·L^{-1} for drinking water and ≤1000 mg·L^{-1} for environmental water bodies) and iron (0.3 mg·L^{-1} for drinking/aquatic ecosystem and 1.0 mg·L^{-1} for effluent)[8,9]. Upon analysis, the AMD assessed in this study exceeded these limits greatly, with sulphate and iron concentrations reaching 9790 mg·L^{-1} and 1421 mg·L^{-1} and extremely high acidity with pH 3.58. These high levels of chemical contamination and extreme acidity emphasized the urgent need for effective treatment strategies.

Traditionally, remediation of AMD was previously focused on conventional treatment processes including neutralization, adsorption, bacterial reduction, ion exchange (IE), and reverse osmosis (RO)[10,11]. However, neutralization and adsorption often generate secondary waste such as sludge requiring further managed and supervised discharge[12]. For example, the AMD neutralization of three shafts in closed mines in Johannesburg, South Africa generate large volumes of sludge which is characterized by leaching of high concentrated metals upon disposal as landfill[13]. Similarly, coagulation which is often applied in conjunction with neutralization is commonly limited by high generation of sludge and low potential for resource recovery. Previously reported membrane technologies explored for AMD remediation include microfiltration (MF), nanofiltration (NF), and reverse osmosis (RO)[14,15]. The RO presented effective removal of particulate matter. Furthermore, the RO offered high quality water recovery with efficient ions

[1]Institute for Nanotechnology and Water Sustainability, College of Science, Engineering and Technology, University of South Africa, Florida Johannesburg, South Africa. [2]AAU Energy, Aalborg University, Aalborg, Denmark. [3]Molecular Sciences Institute, School of Chemistry, University of the Witwatersrand, Johannesburg, South Africa. [4]Center for Membrane Technology, Department of Chemistry and Bioscience, Aalborg University, Aalborg, Denmark.
✉e-mail: nthunln@unisa.ac.za

removal. However, it remains insufficient to remove nitrates[16]. Also, RO is often associated with high operational costs and brine disposal challenges, limiting its sustainability and scalability in AMD treatment[17]. The NF demonstrated high rejection efficiencies for removal of sulphate and heavy metals. However, it is affected by severe membrane fouling, requiring extensive pretreatment[18]. Although water recovery technologies have sought to integrate desalination processes to mitigate water shortages, their high energy requirements, and operational complexities have presented substantial challenges to widespread adoption, particularly in resource-limited countries[19].

Membrane distillation (MD) emerged as a promising thermally-driven separation process capable of treating chemically complex waters[20]. Although it is energy-intensive process because of its dependency on thermal energy, its advantage lies in its capability to operate from low-grade or waste heat, potentially reducing the overall energy requirements when integrated with renewable or industrial waste heat. Dissimilar from high pressure-driven separation RO, the MD utilizes low to moderate temperatures creating a temperature gradient as a vapor driver across a hydrophobic membrane[21,22]. Consequently, only vapor passes through the membrane while rejecting non-volatile solutes. This feature makes MD highly suitable to treat high-salinity and chemically aggressive feedwaters, including AMD[23]. Although the MD has received a remarkable attention in treating high salinity and metal-rich effluents, its industrial adoption is constrained by the energy costs and scaling at high feed temperatures[24]. Integration of crystallization to MD, termed membrane distillation crystallization (MDCr) offers simultaneous recovery of high-purity water and precipitation of valuable mineral salts, thus ensuring zero liquid discharge and circular economy[23,25]. The MDCr presents an opportunity to reduce fouling while recovering resources.

Even though MDCr has prospective industrial applications, it is insufficiently explored as a treatment option for AMD, thereby necessitating the optimum operating conditions in the separation and crystallization processes, including the temperature of the feed and the pH[26]. The composition of AMD vary significantly depending on its source, thus affecting the MDCr process performance due to changes in pH and mineral content[27]. For example, AMD with pH values of 3.58 and 6.47, representing acidic and near-neutral conditions, respectively, poses distinct challenges for membrane degradation, scaling, and crystallization kinetics[28]. Furthermore, while previous studies have established the relevance of MDCr to seawater extraction and efficient industrial brine management[29], its applicability to AMD collected directly from mine shafts (a complex and multi-component effluent) requires rigorous investigation. Most prior studies including our recently reported work focused on synthetic AMD solutions without capturing the multi-component nature and high acidity of the real AMD[30,31]. Environmentally collected AMD differs significantly from synthetic AMD because of its dynamic and complex composition which can potentially affect the membrane performance[32]. For instance, oxidized Fe^{3+} into $Fe(OH)_3$ contributes to membrane scaling while high concentrations of sulphate facilitate gypsum precipitation, further affecting flux stability[33]. Previously reported studies typically used simplified chemical composition which do not represent the intricacies of scaling mechanisms and competitive ion interactions present in real AMD[30,34]. Also, limited studies evaluated the interplay between the feed temperature and pH on MDCr performance to understand their impact on water quality, flux, and crystallization kinetics. For these reasons, in-depth evaluation of AMD in MDCr systems is required to assess the practical feasibility prior to process scale-up, which is the key baseline of the current reported study.

Different from previous studies evaluating the recovery of verily pure water and salts from synthetic feed waters, the current study investigated the novel application of hollow fibre MDCr towards treatment of environmentally collected AMD, with detailed analysis of crystal morphology, composition and water recovery. This practical approach with field environmental AMD strengthened the MDCr applicability for real-world deployment. Specifically, two feedwaters with pH values of 3.58 and 6.47 were collected from the mine shaft (low pH) and the neutralization pond (near-neutral pH) in Witwatersrand Central Basin, Johannesburg, South Africa. Also, the study investigated the influence of feed temperatures (50, 60, and 70 °C) on MDCr performance to assess possible membrane chemical resistance and scaling under the complex chemical matrix and challenging acidic pH of the feed water. Notably, hollow fibre propylene membranes are prone to chemical attach and presented scaling under high operating temperatures, especially when subjected to feed solutions rich in calcium and magnesium sulphates[35]. The integration of crystallization in the membrane distillation (MD) process introduced a transformative approach to valorising AMD as a resource instead of a waste stream. Moreover, the study addressed critical knowledge gaps regarding the operational stability and efficiency of MDCr under variable AMD conditions, advancing the potential for its deployment in real-world scenarios. Also, the influence of feed temperatures on dominant crystallization pathways was critically assessed. By addressing these gaps, this study advances the understanding of MDCr as sustainable AMD treatment within the framework of circular economy.

Results and discussion

Physicochemical characteristics of AMD samples

The AMD from the closed mine shaft decanting into Witwatersrand Basin presented severe water pollution characterized by exorbitant levels of iron, sulphates, phosphates, nitrates, calcium, magnesium and toxic metals above the threshold limits for discharge into environmental bodies (Table 1). The chemical characteristic of this AMD presents an appropriate insight into the environmental impact caused by historical mining activities.

The water sample collected directly from the underground mine shaft was generally acidic with a pH of 3.58. This was consistent with typical AMD characteristics caused by production of sulfuric acid during oxidation of pyrite mineral rocks. The acidic pH triggered mineral dissolution, presenting the significant ionic strength of the water with elevated conductivity of 26,580 $\mu S{\cdot}cm^{-1}$ and total dissolved solids (TDS) of 16999 $mg{\cdot}L^{-1}$. The reported conductivity fell within the reported range (7000 – 155,000 $\mu S{\cdot}cm^{-1}$) from AMD in similar environmental settings[11]. However, the TDS exceeded the desirable limit (500 $mg{\cdot}L^{-1}$) in underground water as well as acceptable limit of 600 $mg{\cdot}L^{-1}$ in drinking water, reflecting high concentration of dissolved solids[36]. This highlighted severe contamination with concerning discharge to the environment. Upon lime neutralization, the AMD pH increased to 6.47, approaching near-neutral conditions, and reduced the solubility of the metal ions, encouraging settling and precipitation of metal hydroxides and sulphates. Subsequently, the conductivity and TDS of the neutralized AMD were reduced, suggesting removal of dissolved ionic metals. However, concentrations remained relatively high prior to coagulation/flocculation.

Based on cationic analysis, the high concentrations, with limited trace elements reflected metal release caused by acidification and dissolution of the minerals. Major cations incorporated Ca^{2+} and Mg^{2+} with high concentration of 2622 and 885 $mg{\cdot}L^{-1}$ respectively. These mineral ions emanated from dissolution of carbonate and silicate minerals, often driven by acidic media. The alkali metal ions, namely Na^{+} and K^{+} presented moderately elevated concentrations of 465 and 156 $mg{\cdot}L^{-1}$ respectively, possibly suggesting dissolution and dissociation from feldspars. Also, interactions with brines from industrial discharge and their infiltration to underground water increased these ions concentrations. Similarly, the AMD presented high levels of Fe^{2+} (1421 $mg{\cdot}L^{-1}$), Mn^{2+} (125.5 $mg{\cdot}L^{-1}$), Al^{3+} (51.5 $mg{\cdot}L^{-1}$), and Cu^{2+} (66.5 $mg{\cdot}L^{-1}$), Ni^{2+} (37.5 $mg{\cdot}L^{-1}$) and Co^{2+} (35.5 $mg{\cdot}L^{-1}$) caused by oxidation of pyrite (a primary mineral rock in the Witwatersrand Gold Reefs and leaching from host rocks such as rhodochrosite and chalcopyrite. Al^{3+} was categorised as non-essential toxic metal because of its high solubility in acidic media, presenting severe neurotoxicity. Also, toxic metals such as Pb^{2+}, Cd^{2+}, As^{2+} were recorded at high concentration of 46, 35, and 31 $mg{\cdot}L^{-1}$ respectively, exceeding their environmental discharge guidelines. This highlighted the significant environmental concern with threatening health risks. Upon AMD neutralization, most metal ions such as Fe^{3+}, Mn^{2+}, Al^{3+}, Cu^{2+}, Ni^{2+}, Co^{2+}, Pb^{2+}, Cd^{2+}, As^{2+} and Ti^{4+} were reduced by 50–90% due to formation of insoluble and settling precipitates. High separation

Table 1 | The Physicochemical characteristics of the AMD from the mine shaft and neutralization pond at Witwatersrand Central Basin Treatment Plant (Germiston closed mine)

Sample ID	Physicochemical parameters										
	pH	Conductivity (µS/cm)	TDS ($mg{\cdot}L^{-1}$)								
Mine shaft	3.58	26,580	16,999								
Neutralized	6.47	16,435	10,427								
	Non-essential metals exhibiting acute or chronic toxicity ($mg{\cdot}L^{-1}$)										
	Al^{3+}	As^{3+}	Cd^{2+}	Co^{2+}	Cr^{3+}	Pb^{2+}	Hg^{2+}	Ag^{+}	Ti^{4+}	Ni^{2+}	Se^{2+}
Mine shaft	51.5	31.1	35.4	35.5	27.7	46.5	9.5	210.5	25.5	37.5	39.6
Neutralized	25.4	11.3	1.5	7.8	9.3	28.1	7.2	8.5	12.7	3.6	23.6
	Essential and slightly toxic metals ($mg{\cdot}L^{-1}$)										
	Cu^{2+}	Fe^{3+}	Mn^{2+}	Zn^{2+}	V^{4+}						
Mine shaft	66.6	1421	125.5	41.6	25.4						
Neutralized	9.2	7.9	13.5	0.4	3.8						
	Alkali and alkali earth metals ($mg{\cdot}L^{-1}$)										
	Li^{+}	Na^{+}	K^{+}	Be^{2+}	Ba^{2+}	Ca^{2+}	Mg^{2+}				
Mine shaft	119.1	464.6	155.4	98.5	3.7	2622.3	884.5				
Neutralized	67.7	382	150.7	4.412	2.3	3048.9	677.9				
	Non-metal ions ($mg{\cdot}L^{-1}$)										
	Cl^{-}	F^{-}	Br^{-}	I^{-}	NO_3^{-}	SO_4^{2-}	PO_4^{3-}				
Mine shaft	1112.8	75.56	64.1	22.7	592.5	9790.2	542.82				
Neutralized	1198.2	49.7	66.5	36.7	578.5	8272.4	253.5				

potential was recorded on alkali earth metals including Be^{2+}, Ba^{2+} and Mg^{2+}. The increased concentration of Ca^{2+} was influenced by addition of lime during neutralization. Notably, alkali metals remained relatively unchanged due to their high solubility. Be^{2+} was grouped under Alkali and alkali earth metals due to its periodic table classification in group II. However, it is worth noting that Be^{2+} is extremely toxic.

Various non-metal ions were monitored to underpin the broad spectrum of the AMD chemical characteristics. The major anions of the acidic AMD (pH 3.58) were SO_4^{2-} and Cl^{-} with extremely elevated concentrations of 9790 and 1113 $mg{\cdot}L^{-1}$ respectively. The domination of SO_4^{2-} confirmed extensive oxidation of sulphide rocks such as pyrite. On one note, the Cl^{-} suggested the mine water interactions with the saline aquifers and discharged industrial effluents. Minor anions with elevated concentrations were NO_3^{-} (592.47 $mg{\cdot}L^{-1}$) and PO_4^{3-} (542.82 $mg{\cdot}L^{-1}$). These ions were extremely high with a possible origination from mining explosives, agricultural runoffs and infiltration from the nearby farm fields. The F^{-}, Br^{-} and I^{-} were present in moderate amounts with concentrations of 75.56, 64.08, and 22.69 $mg{\cdot}L^{-1}$ respectively indicating the leaching from host rocks. The concentration of these minerals presented environmental concerns and possible health challenges experienced by the end-users. Although the chemical characteristics of this AMD aligned with the literature[5], phosphate and nitrates concentrations were highly elevated, potentially influenced by other sources other than mining activities[37]. Upon neutralization, the concentrations of most non-metal ions remained relatively unchanged, with slight reduction of F^{-}, PO_4^{3-}, SO_4^{2-} due to formation of precipitable CaF_2, $Ca_3(PO_4)_2$, $CaSO_4{\cdot}2H_2O$ or $Ca_6Al_2(SO_4)_3(OH)_{12}{\cdot}26H_2O$ in the presence of Al^{3+}. Despite lime dosing at the neutralization pond, the concentration remained high since flocculation was not carried out in this pond. Several suspended and colloidal particles remained in the water phase due to absence of flocculant/coagulant dosing. Additionally, high turbulence and short residence time reduced settling efficiency, leading to high concentrations of metal ions. Despite impressive metal ions reduction, the high concentrations required additional treatment processes such as flocculation, filtration, adsorption and advanced membrane processes. This necessitated further investigation with comprehensive environmental monitoring to establish improved remediation strategies including MDCr.

Effect of feed temperature on water flux and salt rejection

Figure 1 presents the performance of membrane distillation-crystallization (MDCr) system for treating acidic AMD. Based on temperature profiles, the permeate flux was higher (3.3 $kg{\cdot}m^{-2}{\cdot}h^{-1}$) at high operating temperatures (70°C) compared to 2.2 and 1.3 $kg{\cdot}m^{-2}{\cdot}h^{-1}$ at 60 °C and 50 °C respectively, especially for pH 3.58 feed water. This was motivated by enhanced temperature difference (deltaT) acting as a driving force for vapor transport, typically 25.1, 22.7 and 18.5 at 70, 60 and 50 °C respectively. At 70 °C, the permeate flux of the near-neutral (pH 6.47) feed water reached an approximate peak of 4.0 $kg{\cdot}m^{-2}{\cdot}h^{-1}$ which was higher than 3.3 $kg{\cdot}m^{-2}{\cdot}h^{-1}$ recorded for acidic pH 3.58. Similar patterns were recorded across all feed temperatures, demonstrating a positive impact on flux at high pH values. The flux reduction at low pH values compared to near-neutral was associated with increased fouling induced by precipitation of heavy metal ions at high acidic conditions. Similar findings were reported by Charfi et al.[38]. where membrane surface interaction and fouling propensity were influenced by pH and the presence of specific metal cations such as Ca^{2+} and Fe^{3+}, which are abundant in AMD[38]. The permeate flux remained relatively stable at low water recovery factors (until 70%) for all feed temperatures. Based on temperature profiles, vapour gradient remained relatively stable at lower feed temperatures, thus maintaining the stability of the permeated flux. Although high feed temperature (70 °C) improved permeate flux, severe flux decline was recorded at high recovery factors above 70%. This was accelerated by gypsum scaling due to the presence of high Ca^{2+} and SO_4^{2-} concentrations. Despite a flux decline at high recovery factors during operations with high temperatures (70 °C), the flux remained relatively stable at high recovery factors (>70%) during operations with low feed temperatures (60 and 50 °C). Notably, deltaT (also known as temperature difference or a measure of thermal gradient across the membrane which influence vapour transport in MDCr systems) remained relatively stable at low recovery factors (≤60%). However, this considerably increased at high recovery factors (>60%) for all feed temperatures and pH values. Various factors were associated with increased deltaT at high recovery factors. This includes accumulation of solutes near the membrane surface increasing local concentration gradient, thus elevating the temperature on the feed side due to reduced thermal conductivity of the feedwater. Also, the increase in

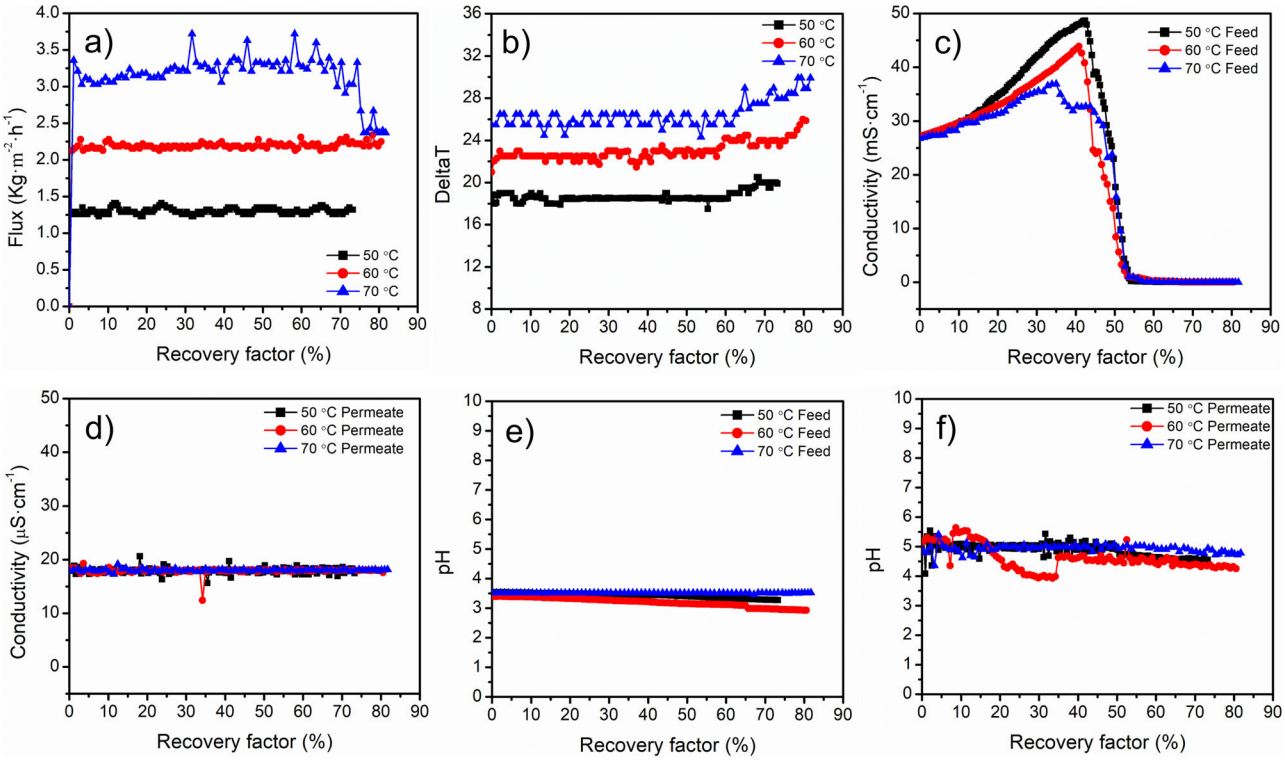

Fig. 1 | MDCr Process performance evaluation towards treatment of pH 3.58 feed water. a flux, **b** deltaT also known as temperature difference, **c** feed conductivity **d** permeate conductivity, **e** feed pH, and **f** permeate pH, all changing as function of recovery factor.

solute concentration at the membrane interface altered the vapor pressure and energy requirements for phase change. Similar trend was reported upon membrane scaling which reduced the heat transfer efficiency, causing a higher feed-side temperature[39]. It is worth noting that the feed flow rate decreased at high recovery factors due to low volumes available in the feed tank. The decreased feed circulation reduced the convective heat transfer, causing a rise in temperature on the feed side of the membrane, thus increasing deltaT. Based on deltaT changes, the MDCr process was affected by temperature polarization effects which reduced the efficiency and stability of vapour flux. These polarization effects were influenced by formation of thermal boundary layer at the interface of the membrane which limited heat transfer, reducing the effectiveness of temperature difference across the membrane[40]. These reduced convective heat transfer became more pronounced at high recovery factors (>70%) as the crystal salts were accumulating at the membrane interface. The increased deltaT at high recovery factors suggested formation of boundary layer, reducing thermal efficiency as crystallization progressed[41]. This could be ascertained in future studies utilizing the computational fluid dynamics modelling to quantify the effects of feed conditions on temperature polarization effects. Although minor flux decline was recorded due to increased feed concentrations at high recovery factors which reduced water activity, the stability reported in Figs. 1 & 2 was associated with continuous crystallization in MDCr. During salt precipitation, the osmotic pressure in the feed does not increase as critically as in concentration affected processes like RO. Also, the stable deltaT at high recovery factors sustained vapour pressure differentials, ensuring minimum flux declines[42]. Temperature differences across the membrane were mirrored between the acidic and near pH feed waters for all temperatures, with pH 6.47 remaining stable and exhibiting slightly lower values at 50 °C feed temperature (Fig. 2). The lower deltaT was linked to steric hindrance of heat transfer induced by compromised thermal efficiency of fouled membrane.

The feed conductivity increased with recovery, reflecting the salts becoming concentrated in the retentate. The sharp increase took place at low recovery factors until 34.9, 40.8 and 42.4% at 70, 60 and 50 °C feed temperatures respectively. The peak conductivity values recorded were 36,890, 43,910 and 48,679 $\mu S \cdot cm^{-1}$ at pH 3.58. The values were smaller at pH 6.47, influenced by the presence of insoluble hydroxides at similar recovery factors. This implied high ions dissolution at low pH, influencing the crystallization kinetics. However, at high pH (6.47), the ion solubility decreased due to formation of hydroxides and carbonates characterized by low solubility constants. Above the mentioned recovery factors, the feed conductivity declined abruptly, citing the decrease in free mobile ions caused by supersaturation and formation crystal salts. This suggested that salt concentration was a limiting factor at high recoveries, potentially influencing the crystallization. Crystal formation causing a sharp decline in feed conductivity was confirmed through in-situ analysis using optical microscopy. The hypothesis of conductivity reduction caused by salt precipitation rather than dilution effects were further confirmed by reported increase in mean crystal sizes. Also, the formed crystals were confirmed through XRD analysis. The permeate conductivity remained relatively low for both pH conditions ($\leq 19\ \mu S \cdot cm^{-1}$), confirming the MDCr process effectiveness towards removal of dissolved ions (99.9% salt rejection). The feed pH remained relatively stable with a slight decline from 3.58 at zero recovery to 3.52, 3.20, 2.93 at highest recovery as per 70, 60 and 50 °C feed temperatures respectively for pH 3.58. The slight decrease in feed pH was influenced by increased concentration of the hydrogen ions (an indicator of feed acidity). Also, the pH stabilized approximately at 6 for a feed pH of 6.47, suggesting an unchanging solution chemistry. However, the permeate pH decreased slightly at high recovery factors for all feed temperatures and pH values. This was caused by preferential transport of the volatile acidic components as suggested by previous findings[43,44]. Although no direct analysis of volatile species was carried out in this study, literature reported partial volatilization of weak acids such as H_2CO_3 and H_2SO_4 at high temperature, promoting diffusion and acidification of the permeate[45]. This aligned with reported literature in MD systems where produced CO_2, NH_3 and SO_2 increased the permeate acidity[45]. However, the overall pH shift remained minimal, confirming the effectiveness of MDCr towards stabilizing the bulk chemical composition of the permeate. Despite detailed records in slight permeate contamination where changes in acidity and mineral ions were reported, the

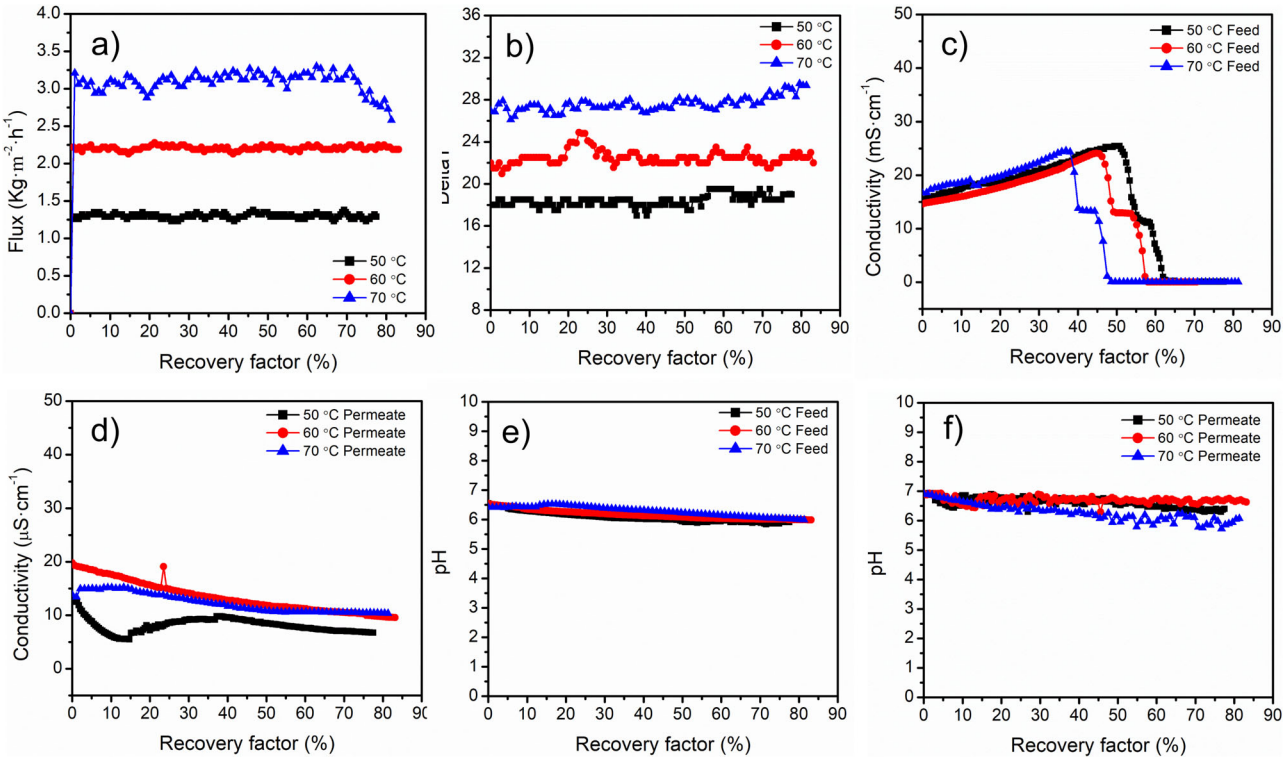

Fig. 2 | MDCr Process performance evaluation towards treatment of pH 6.47 feed water. a flux, **b** deltaT also known as temperature difference, **c** feed conductivity **d** permeate conductivity, **e** feed pH, and **f** permeate pH, all changing as function of recovery factor.

hollow fibre MDCr demonstrated excellent performance, achieving high water recoveries (>80%) with relatively stable fluxes and efficient salt rejections. Based on feed temperatures, 60 °C was preferred due to moderately stable permeate flux. In summary, the neutralized feed water (pH 6.47) presented better performance in terms of flux and temperature gradient across the membrane compared to the acidic feed water (pH 3.58) due to minimized fouling. This highlighted the importance of feed neutralization prior MDCr, particularly in high recovery scenarios. In case of prioritizing mineral salts recovery, pH 3.58 was preferred towards recovery of precious metals.

While the permeate flux was relatively stable at high recovery factors, long-term industrial operation of MDCr may be affected by scaling/inorganic fouling, particularly in acidic conditions (pH 3.58)[46]. The current MDCr system demonstrated stable performance over short periods of operation. However, inorganic fouling is prominent in long-term continuous treatment conditions, especially under high recovery and high temperature conditions. Interestingly, the MDCr system demonstrated high resistance to salt rejection decline despite reports of PP membranes to be prone to wetting and degradation when exposed to low pH feed solutions, especially when operated over prolonged durations[47]. Under long-term continuous operations, these issues could impact flux and selectivity stability. To stabilize their performance in long-term operations, surface modifications with superhydrophobic and chemically resistant materials is recommended. Also, regular cleaning protocols should be carried out to mitigate irreversible inorganic fouling. These considerations are vital in MDCr process upscaling in remediation of real AMD.

Morphology of crystal structures

Morphological properties and crystal structures of the formed salts under varying feed temperatures and feed waters of differing pHs is presented in Fig. 3: Initially formed crystal structures were sparsely and poorly defined across all temperatures, particularly where acidic water (pH 3.58) was used as feed. The acidic conditions favoured nucleation and growth, resulting in largely pronounced and aggregated crystal salts. The particles remained localized with irregular shapes. At pH 6.47 and initial growth, the crystals were relatively abundant and evenly distributed, noticeably with elongated and branched forms towards the final growth phase. The near-neutral conditions (pH 6.47) suppressed formation of large particles, particularly due to crystal compaction. These compact structures were influenced by differences in ion paring, lattice energy effects and nucleation sites. For example, Ca^{2+} and Mg^{2+} ions formed dominating compact gypsum and ettringite due to their strong lattice interactions at near-neutral conditions[48]. Also, AMD neutralization promoted saturation of calcium and sulphate ions, which increased likelihood of heterogenous nucleation at membrane interface, resulting in formation of compact morphologies. At low feed temperatures (50 °C), the crystal salts exhibited smaller sizes with even distribution, suggesting low rate of supersaturation and growth. The crystal salts were more pronounced at 60 °C with larger and dense structures for all pH levels. Thus, the distribution increased with temperature, presenting a more uniform and dense distribution. Upon increasing the feed temperature further to 70 °C, the crystal salts displayed highest level of aggregation with structural complexity, especially at pH 6.47. The elongation and branching of compact crystal structures at pH 6.47 suggested potential formation of calcium/magnesium sulphates and carbonates with predominantly elongated and branched structures. At pH 3.58, large crystal particles suggested process favouring formation of transition metal salts under acidic conditions.

Effect of pH and feed temperature on crystal salts growth rate

In MDCr processes, the pH and temperature play a critical role in influencing the crystal growth rates and size[30,44]. For these reasons, the interplay between pH and temperature requires a careful control to achieve desired crystal size distributions, morphology. Therefore, adjusting these parameters is crucial in tailoring the crystal properties. Although the impact of various feed temperatures on crystal formation was evaluated, the acidic and near-neutral feed waters were used as collected from the mine area without further chemical alterations. The influence of both temperature and feed pH provided insightful performance of the MDCr process towards treatment of AMD.

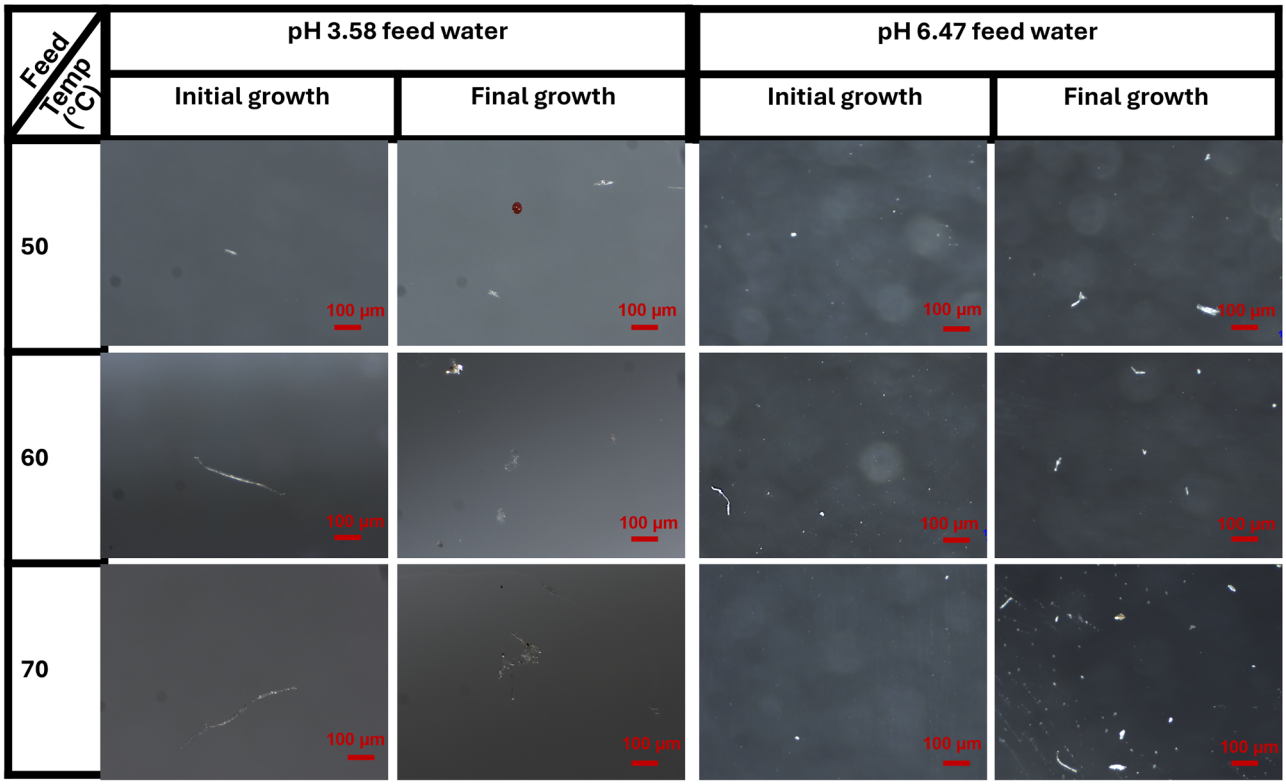

Fig. 3 | The effect of feed temperature on morphological properties of crystal salts at various growth phases, namely initial, continuous and final. Two AMD feed solutions with pH 3.58 and 6.47 were used.

Fig. 4 | The effect of pH and temperature on the crystal salts formation and growth. a pH 3.58, and **b** pH 6.47.

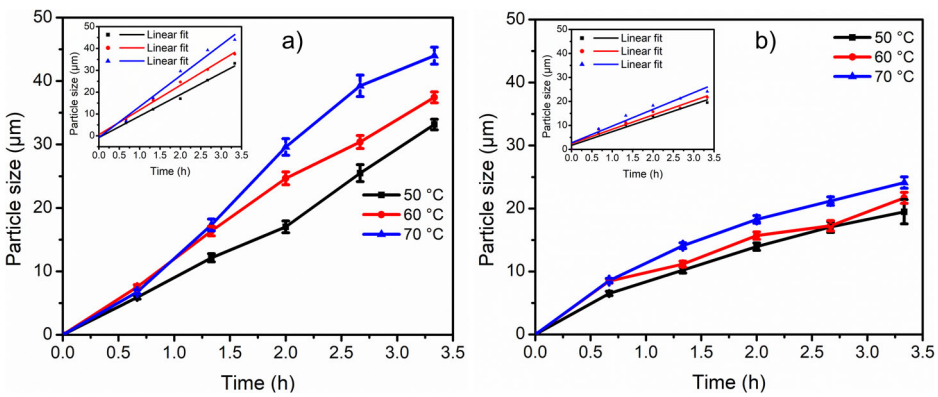

The findings of the investigated formation and growth of crystals salts are presented in Fig. 4: The formation of the crystals began at recovery factors between 35% and 45% for both pH conditions feed waters. Based on plot insert in Fig. 4, the particle growth for both pH values followed a linear fit with correlation coefficients (R^2 = 0.94–0.99), suggesting a steady-state crystallization kinetics during the recording timeframe. Comparable behaviour was reported by Zheng et al.[49] where particle size growth followed a linear trajectory under controlled crystallization processes[49]. However, these conditions require extensive research in MDCr processes for conclusive findings. Elevating the feed temperature increased the crystal growth rate. The sizes of the crystal salts reached 40–45 µm and 19–22 µm from feed waters of pH 3.58 and 6.47 respectively within 3.5 h at the highest feed temperature 70 °C. At 50 °C, the maximum crystal sizes were smaller, specifically ~33 µm and ~19 µm from of pH 3.58 and 6.47 feed waters respectively. At higher temperatures, faster ion diffusion was facilitated, enhancing the nucleation and growth kinetics. According to Yadav et al.[50], the elevated temperature improves the ionic mobility and diffusion leading to faster crystal growth[50]. Similarly, Mapetere et al. (2025) reported an accelerated ionic mobility upon increasing the feed temperature, leading to rapid supersaturation and enhanced nucleation rates[51]. These findings supported the reported large crystal formation and faster growth rates at high temperatures.

In classical nucleation theory, temperature increase promotes high nucleation rate, forming greater number of clusters with small crystal sizes[52]. However, the current reported findings deviated from classical crystallization theory where larger crystals were formed at higher temperatures. This deviating trend was associated with selective crystallization mechanisms in AMD, where metal-sulphates interactions were primarily responsible for growth kinetics. Also, the crystal impurities at high temperatures suppressed the secondary nucleation, favouring formation of fewer and larger crystals instead of many and smaller[53]. The ICP analysis of crystal salts confirmed the presence of metal-rich particles which altered growth

dynamics. Based on growth patterns, the crystal growth of pH 6.47 feed water was slightly slower with growth rates of 2.85, 2.98 and 3.49 μm·h^{-1} at 50, 60, and 70 °C feed temperatures respectively compared to 4.92, 5.66, and 7.07 μm·h^{-1} recorded from pH 3.58 feed water (Table 2). Slower growth rates at pH 6.47 were attributed to predominant formation of calcium carbonate crystals which are more compact and dense structures[54]. In contrast, the large crystals recorded at pH 3.58 were formed due to precipitation of metal-rich salts such as iron sulphates, and aluminium nitrates with higher solubility limits in acidic conditions. Upon crystallization, these salts formed large particles. Other factors such as rate of nucleation and lattice structure played a significant role in sizes of crystal formed. Because of high metal solubility at pH 3.58, the rate of nucleation was reduced, promoting formation of large crystals before new nuclei formed. Also, sulphate complexes such as $FeSO_4$ and $Al_2(SO_4)_3$ crystalized into structures with low nucleation densities, favouring growth of crystals over dispersion[55,56]. Furthermore, the crystal sizes were influenced by lattice energy. For instance, metal sulphates which exhibit low binding energies compared to calcium salts facilitated larger crystal formation[55]. These combined effects contributed to different crystal growth patterns between acidic and neutralized AMD. Although particles growth patterns were significantly different upon treatment of feed waters with acidic and near-neutral conditions, the recorded particle sizes (6–44 μm) fell within reported findings where MDCr processes produced crystal sizes (4–50 μm) depending on feed chemical characteristics and process operational conditions[57].

Table 2 | The crystal growth rates obtained from different feed temperatures and pH values, derived from the linear plots as defined by the R^2 values and linear equations

Feed temperature (°C)	Growth rates of crystals salts and linear correlation			
	pH 3.58 (μm·h^{-1})	R^2	pH 6.47 (μm·h^{-1})	R^2
50	4.92	0.99	2.85	0.97
60	5.66	0.99	2.98	0.94
70	7.07	0.98	3.49	0.94

Effect of pH and feed temperature on crystal size distribution

The crystal size distribution of the produced salts from the acidic feed water (pH 3.58) and near-neutral (6.47) are reported in Fig. 5: The crystal began to form upon nucleation prompted by supersaturation (typically at higher water recovery factors). At pH 6.47, the crystal size distributions presented narrow peaks with sizes ranges (6.9–22.5 μm) suggesting dominance of smaller and dense crystals. At high pH, salts such as calcium and magnesium with low solubility formed dense and compact salt structures. These trends aligned with classical nucleation theory where ion mobility and saturation index controlled the rate of crystal growth[55]. However, peak broadening of crystal sizes (5–50 μm) was evident at pH 3.58 potentially with dominance of heavy metal sulphates and oxides under acidic conditions. The high solubility of sulphates and oxides promoted formation of large and metal-rich crystal induced by electrostatic interactions between the cation and anion in acidic conditions. At lower feed temperatures (50 °C), the size distribution was narrow, favouring the formation of small particle size. This was driven by slow nucleation and growth dynamics. The particle size distributions shifted towards larger crystal sizes at higher temperatures (70 °C) for both acidic and near-neutral feed waters. This trend aligned with the faster ion diffusion to nucleation accelerating the growth kinetics. Enhanced kinetic energy with reduced viscosity at higher temperatures facilitated ionic mobility and diffusion favouring formation of large crystal salts. However, excessive temperature elevation affected the width of metastable zone, resulting in formation of amorphous precipitates, rather than well-defined crystal salts. For this reason, optimization of feed temperature and pH is key to achieve desired crystal purity and morphology.

On one hand, crystal size distributions broadened with a greater fraction of large particles at higher recovery factors (>50%) for all feed waters and temperatures. This was consistent with the reported findings where prolonged cycling of feed supersaturation induced coalescence from secondary growth of the crystals[58,59]. Also, the production of wide range of crystal sizes at higher recovery factors was influenced by agglomeration

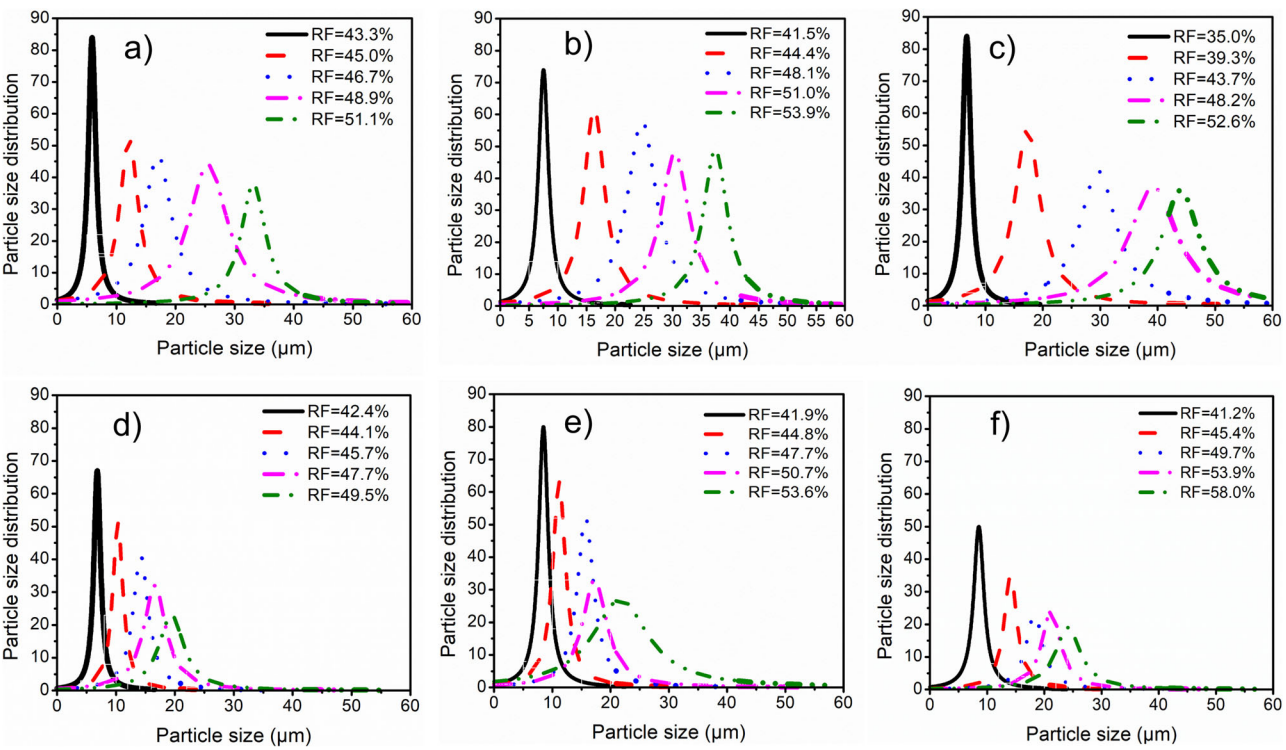

Fig. 5 | Formation and growth of crystal salts evaluated from MDCr under varying feed water recovery. The impact of feed temperature on growth stages of particle was analysed, notably **a** 50 °C, **b** 60 °C **c** 70 °C for pH 3.58 feed water, **d** 50 °C, **e** 60 °C **f** 70 °C, for pH 6.47 feed water.

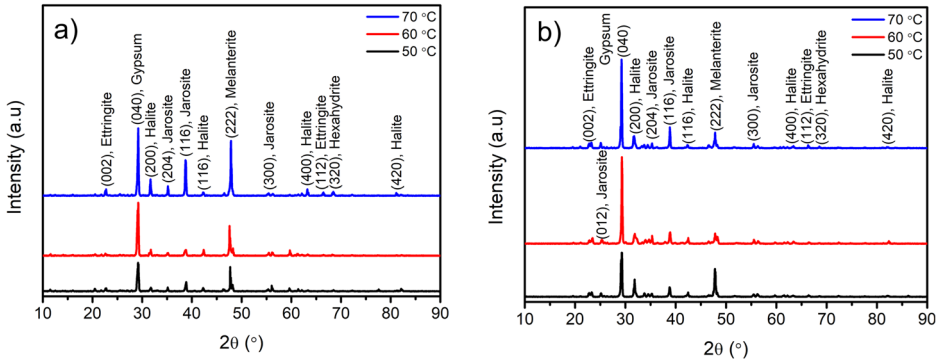

Fig. 6 | XRD patterns. The XRD patterns of the crystal salts produced from MDCr with varying feed temperature (50, 60 and 70 °C) where AMD feed waters with **a** pH 3.58 and **b** pH 6.47 were used.

Table 3 | Crystallographic system identification of the crystal salts produced from AMD feed solutions of pH values 3.58 and 6.47

2Θ (°)	Miller indices (hkl)	JCPDS card	Identified salt	Crystal system
22.7	002	41-1451	Ettringite: $Ca_6Al_2(SO_4)_3(OH)_{12}{\cdot}26H_2O$	Hexagonal
25.4	012	36-0429	Jarosite: $KFe_3(SO_4)_2(OH)_6$	Hexagonal
29.2	040	21-0816	Gypsum: $CaSO_4{\cdot}2H_2O$	Monoclinic
31.7	200	05-0628	Halite: NaCl	Cubic
35.2	204	36-0429	Jarosite: $KFe_3(SO_4)_2(OH)_6$	Hexagonal
38.7	116	36-0429	Jarosite: $KFe_3(SO_4)_2(OH)_6$	Hexagonal
42.3	220	05-0628	Halite: NaCl	Cubic
47.9	222	21-0888	Melanterite: $FeSO_4{\cdot}7H_2O$	Monoclinic
56.2	300	36-0429	Jarosite: $KFe_3(SO_4)_2(OH)_6$	Hexagonal
63.2	400	05-0628	Halite: NaCl	Cubic
66.5	112	41-1451	Ettringite: $Ca_6Al_2(SO_4)_3(OH)_{12}{\cdot}26H_2O$	Hexagonal
68.4	320		Hexahydrite: $MgSO_4{\cdot}6(H_2O)$	Monoclinic
81.1	420	05-0628	Halite: NaCl	Cubic

Three feed temperatures, namely 50, 60 and 70 °C were evaluated to analyse their impact on crystal salts formation.

under high rates of supersaturation conditions. The narrow peaks at lower recovery factors (35 – 45%) were influenced by formation of monodispersed crystals predominantly due to limited nucleation and crystal growth. Summarizing the practical implications of crystal formation, the pH 6.47 was preferred for sustainable operations where narrow size distributions are required. However, the acidic condition (pH 3.58) is important towards recovery of valuable salts like iron oxides, though additional separation technology is required for specific resource recovery to reduce wide dispersion of formed salts and to improve their economic value.

XRD analysis of the recovered mineral salts

X-ray diffraction (XRD) patterns of the MDCr-processed crystal salts produced from feed waters of different pH values and varying feed temperatures were analysed to determine the dominant salts formed, their lattice structures, and their crystallographic parameters (Fig. 6). Recorded diffraction peaks corresponding to various crystal salts and their lattice system are presented in Table 3. Based on XRD patterns, the dominant salts collected from pH 3.58 feed water for all temperatures were gypsum, jarosite, ettringite, halite, melanterite and hexahydrite. However, jarosite was more pronounced at elevated temperatures (60 °C and 70 °C) induced by abundant Fe^{3+} and SO_4^{2-} ions at acidic conditions. Similarly, melanterite formation was induced by iron-rich feed water at low pH. Based on feed water characteristics, the concentrations of Ca^{2+}, Fe^{3+}, SO_4^{2-}, Al^{3+} were 2622, 1421, 9790.23 and 51.5 $mg{\cdot}L^{-1}$ respectively facilitating abundant formation of these crystal salts at low pH. Ettringite and Halite presented sharper peaks compared to others indicating higher crystal lattice purity with improved crystallinity at pH 3.58. At pH 6.47, the dominant salts were halite, ettringite, hexahydrite and jarosite. Abundance of Ettringite was facilitated by high concentrations of calcium and moderate levels of aluminium. However, jarosite intensity was slightly reduced due to minimal solubility of Fe^{3+} at higher pH. Compared to neutralization, the MDCr does not only facilitate the recovery of high-quality water with 99.9% salt rejection, but enabled selective recovery of mineral salts such as gypsum, halite and ettringite. In contrast, neutralization generate large sludge presenting disposal challenges, despite its effectiveness for bulk removal of acidity and metals[60]. The dual functionality of MDCr reduced the waste and enabled valorisation of minerals, supporting the objectives of zero liquid discharge (ZLD) and alignment to circular economy.

The identified salts span from a variety of crystal lattice systems where Jarosite and Ettringite dominated with hexagonal crystal structures in both pH 3.58 and 6.47 feed waters (Table 3). Jarosite was more intense at low pH, showcasing its dependence on acidic SO_4^{2-} and Fe^{3+}-rich environments. Monoclinic structures were melanterite, hexahydrite and gypsums dominating in acidic conditions, though gypsum was prevalent in both pH values. Cubic halite was prevalent in both feed conditions, though increased significantly in neutral environments as evidenced by the sharper diffraction peaks. The reported findings aligned proficiently with literature where jarosite formation was dominant in acidic environments, while halite dominates at near-neutral pH values and elevated temperatures during thermal evaporation of AMD. Likewise, ettringite is prevalent at neutral conditions during AMD treatment with lime[61]. Although the XRD results confirmed formation of well-defined crystalline structures such as halite and ettringite at pH 6.47 and jarosite at pH 3.58, minor amorphous phases were detected, suggesting the none-crystalline impurities. Therefore, further process optimization including controlled crystallization and post-processing techniques including recrystallization and selective crystallization are recommended to improve the purity of the recovered salts. Also, trace amounts of toxic metals such as Pb, As and Cd, could prohibit the direct use of the recovered salts in some applications. Therefore, future studies should explore pre-treatment separation techniques with high ion-selectivity to improve the purity of the recovered crystal salts.

The chemical analysis of the produced crystal salts

The experimental results showed good salt rejection performance (99.9%), enabling potential crystal recovery from real AMD. The Witwatersrand Central Basin where the tested AMD was collected discharges approximately 15 million litres of AMD per day, primarily from the shaft pump station. This high-volume discharge opens a substantial evaluation of MDCr at industrial scale. However, the high MDCr energy demand presented operational cost implications, requiring an offset from integration of renewable heat sources such as solar energy or industrial waste heat to improve feasible deployment of this technology. The tested feed

temperatures and source of the AMD presented varying impact on the amount of crystal salts produced from MDCr (Table 4) and their chemical composition (Table 5). At pH 3.58 feed water, the mass of the salts increased with rising temperatures, reaching 18.51 ± 1.19 g at 70 °C. This was linked to MDCr efficiency and crystallization kinetics at higher temperatures, where elevated vapour pressure facilitated faster particle growth while ensuring high salt rejection. Conversely, the pH 6.47 feed water exhibited non-linear response, with the highest amount of salts (18.52 ± 1.29 g) produced at 60 °C. The mass balance analysis was performed in relation to the obtained mass of crystallized salts, where 1.0 L AMD feed volume with conductivity of 26,580 $\mu S \cdot cm^{-1}$ and TDS of 16,999 $mg \cdot L^{-1}$, equated to approximately 17.0 g of solutes entering the MDCr system. The crystallized salts recovered from the MDCr matched the TDS closely, with masses of 17.03 g (50 °C), 17.46 g (60 °C), 18.51 g (70 °C) at pH 3.58 and 17.63 g (50 °C), 18.52 g (60 °C), 17.48 g (70 °C) at pH 6.47. The mass of crystallized salts was slightly higher than the mass input (exceeding by 1.7–9.0%) due to co-precipitation of impurities such as water inclusion in the hydrate forms and experimental variability. These recoveries aligned with the feed TDS, confirming the complete recovery of crystallized salts through MDCr. Also, the achieved water recovery factors of 82%, 81% and 73% at feed temperatures of 50, 60 and 70 °C corresponded to 0.82, 0.81 and 0.73 kg. The unrecovered 0.18–0.27 kg (18.0–27.0%) of AMD feed water was retained as dead volume within the membrane module and tubing, with minimal losses of water leakage in the form of vapour. These results demonstrated strong process mass balance, highlighting the effectiveness of MDCr in dual recovery of mineral salts and high-purity water from the AMD without notable resource losses.

Based on collected crystal salts from MDCr, the study reported on chemical composition based on classified toxic, essential alkali/alkaline earth and non-metallic ions and trends in crystallization (Table 5). The

Table 4 | The mass of crystal salts produced from 1.0 L of pH 3.58 and 6.47 feedwaters through MDCr, where three process temperatures were monitored

Feed pH	MD operating feed Temp (°C)	Mass of crystal salt (g)
pH 3.58	50	17.03 ± 1.28
	60	17.46 ± 1.07
	70	18.51 ± 1.19
pH 6.47	50	17.63 ± 0.97
	60	18.52 ± 1.29
	70	17.48 ± 1.14

Table 5 | The chemical composition of crystal salts produced from pH 3.58 and 6.47 feedwaters through MDCr, where three process temperatures were monitored

		Toxic and nonessential metal ions ($mg \cdot L^{-1}$)									
Feed pH	MD Operating Temp (°C)	Al^{3+}	As^{3+}	Cd^{2+}	Co^{2+}	Cr^{3+}	Pb^{2+}	Hg^{2+}	Ag^{+}	Ni^{2+}	Se^{2+}
3.58	50	91.70	25.17	5.394	16.18	16.18	34.16	25.17	169.0	12.58	57.53
	60	95.29	32.36	8.990	25.17	21.57	25.17	34.16	186.9	8.990	84.50
	70	75.51	28.77	3.596	21.57	19.77	37.76	37.76	208.5	10.79	95.29
6.47	50	100.6	16.18	3.596	16.18	12.59	28.77	19.78	219.3	5.397	52.14
	60	70.12	19.77	1.798	14.38	10.79	12.59	16.18	233.7	7.192	70.12
	70	79.11	21.58	5.394	19.75	14.35	23.37	21.57	239.1	1.798	39.55
		Essential metals and toxic at elevated concentrations ($mg \cdot L^{-1}$)									
		Cu^{2+}	Fe^{3+}	Mn^{2+}	Zn^{2+}	V^{4+}					
3.58	50	32.36	37.75	16.18	1.798	14.38					
	60	25.17	66.52	10.79	8.990	19.77					
	70	39.56	52.14	19.77	5.394	16.18					
6.47	50	23.37	28.76	5.39	3.596	7.192					
	60	25.17	14.38	1.79	1.798	8.990					
	70	19.79	32.36	3.60	1.798	3.596					
		Alkali metal and alkali earth ions ($mg \cdot L^{-1}$)									
		Li^{+}	Na^{+}	K^{+}	Be^{2+}	Mg^{2+}	Ca^{2+}	Ba^{2+}			
3.58	50	122.3	417.1	147.4	16.18	773.8	3477	8.990			
	60	120.5	402.8	149.2	10.79	642.5	2709	3.596			
	70	129.4	427.9	158.2	8.990	667.1	1880	7.192			
6.47	50	138.4	458.5	188.7	1.798	725.8	6553	3.596			
	60	115.0	499.8	195.9	7.192	599.3	7467	5.394			
	70	124.1	442.3	169.0	3.596	452.8	7163	1.798			
		Non-metal ions ($mg \cdot L^{-1}$)									
		Cl^{-}	F^{-}	Br^{-}	I^{-}	NO_3^{-}	SO_4^{2-}	PO_4^{3-}			
3.58	50	1116	116.9	BDL	BDL	845.1	9601	503.4			
	60	1010	133.1	BDL	BDL	91.69	10662	557.3			
	70	1229	124.0	BDL	BDL	73.71	10500	59.33			
6.47	50	981.7	97.09	BDL	BDL	88.10	11957	48.54			
	60	787.5	89.54	BDL	BDL	66.52	12101	43.15			
	70	960.2	89.36	BDL	BDL	79.11	10770	53.94			

change in pH and feed temperature presented a significant variation in concentrations of the toxic metal ions. For instance, the concentration of Pb^{2+} was noticeably higher (37.76 mg·L^{-1}) at pH 3.58 compared to 28.77 mg·L^{-1} at pH 6.47. This observation suggested higher dissolution in acidic environments. Similarly, the higher concentrations of most toxic metal ions including As^{3+}, Cd^{2+}, Hg^{2+} peaking at 70 °C proved enhanced solubility and precipitation kinetics increasing with temperature. However, the concentrations of most toxic metal ions were generally lower across all temperatures, reflecting enhanced crystallization of hydroxides and carbonates at near-neural pH. Compared to Table 1, concentrations of the produced metal ions differed significantly with some presenting reductions while some were enriched. For example, the concentration of Al^{3+} from raw AMD was 51.5 mg·L^{-1} while the crystal salt at 60 °C reached 95.29 mg·L^{-1}, suggesting selective crystallization.

Other metal ions presenting high concentrations in acidic conditions (pH 3.58) were Fe^{3+} (66.52 mg·L^{-1} at 60 °C), Cu^{2+} (39.56 mg·L^{-1} at 70 °C), Mn^{2+} (19.77 mg·L^{-1} at 70 °C) compared to their counterpart ions in near-neutral conditions (pH 6.47). However, their low concentrations from the crystal salts compared to their high concentrations in AMD (for example, 1421 mg·L^{-1} of Fe^{3+}) was associated with metal reduction during precipitation and sand filtration pretreatment prior MDCr operations. However, the concentration of Ca^{2+} was higher at near-neutral conditions (pH 6.47), reaching 6553 mg·L^{-1} compared to 3477 mg·L^{-1} at pH 3.58 during salt crystallization at feed temperature of 50 °C. The increase in Ca^{2+} was influenced by lime dosing during AMD neutralization, achieving the feed pH of 6.47. The SO_4^{2-} dominated the fraction of non-metal ions, with concentrations reaching 10,000 mg·L^{-1} for all pH values and temperatures. This was linked to preferential crystallization with high metal ions concentration such as Ca^{2+}, particularly at near-neutral feed conditions (pH 6.47). Although Cl^- ions presented minimal variations with temperature, their concentration was higher (1229 mg·L^{-1}) at feed pH and temperature of 3.58 and 70 °C suggesting minimal co-precipitation. Compared to Table 1, the concentrations of NO_3^- dropped significantly, probably due to thermal decomposition during MDCr. Based on these findings, the MDCr paved the way for specific ion recovery, though intensive optimization of the process conditions and feed pre-treatment are required towards improved circular economy strategies. For instance, the recovered halite could potentially be used in road de-icing while ettringite could find a potential application in construction materials. Despite the mentioned potential applications, the MDCr operational costs should be compared with the market value of the recovered salts to conclude their economic feasibility. Similarly, techno-economic analysis comparing MDCr, RO and lime neutralization should be carried out to determine the cost-benefit ratio.

Reflecting on the overall findings, the current study evaluated the feasibility for simultaneous water purification and mineral salts crystallization from AMD of differing pH values through MDCr. The neutralized feedwater (pH 6.47) facilitated formation of smaller, dense crystals. At acidic conditions (pH 3.58), valuable metal-rich crystal salts were obtained. However, robust membranes are critically required to sustain low pH conditions for long-term operations. Also, 60 °C presented optimal operating feed temperature, presenting flux stability, energy efficiency and crystallization kinetics. The findings highlighted the transformative behaviour of MDCr in converting AMD into valuable resources, aligning with circular economy by addressing water scarcity and mineral shortages. Also, application of MDCr to treat real AMD with varying chemistry offered the insight into technology novelty. The dual benefit of water recovery and salt crystallization with minimal mass loss and near-complete ion rejection (99.9%) highlighted the robustness of polypropylene hollow fibre membranes in challenging environments like AMD treatment while emphasizing the importance of optimizing operating conditions to mitigate fouling and scaling. This provided a meaningful contribution to advancing the laboratory MDCr concept to field applicable technology. Nonetheless, the pilot-scale validation through field trials is critically important to validate laboratory findings to ensure scalability. This will contribute to the scientific advancements of the MDCr while aligning with global efforts to promote circular economy and sustainable water management in mining-impacted regions. Also, selective mineral extraction and integration of renewable energy should be considered to enhance process sustainability.

Methods

Materials and feed water samples

The AMD samples were collected from the Central Basin AMD Treatment Plant in Germiston, within the Witwatersrand mining region, South Africa. Prior to development of a treatment plant, this site was known to decant the untreated AMD, historically linked to closed gold mine operations. Currently, the Central Basin pumping station discharge approximately 15 million litres of AMD per day downstream. Precise geographic coordinates of sampling area identified using civilian-grade Global Positioning System (GPS) with a ± 5 m horizontal accuracy were −26.2176° latitude, 28.1742 longitude. Two untreated AMD water samples were collected to assess the MDCr process performance under different conditions: A highly acidic AMD (pH 3.58) directly from the mine shaft, and partially neutralized (pH 6.47) from lime-treated holding pond. The samples were collected in airtight high-density polyethylene (HDPE) containers, purged with nitrogen and transported to the laboratories under refrigerated conditions (4 °C) to minimize oxidation.

Physicochemical properties such as pH, conductivity, total dissolved solids (TDS) were measured onsite using Bante900 potable multiparameter water quality meter (Table 1). The concentration of the cations namely, Li, Na, K, Ca, Mg, Al, Mn, Fe, Ag, Cu, Ni, Co, Pb, Zn, Cd, As, Cr, Ti, V was analysed using Spectro Genesis inductively coupled plasma optical emission spectroscopy (ICP OES), equipped with Smart Analyzer Vision Software. A mixed standard containing the above-mentioned cations was used as a stock solution to prepare a series of 0.00, 0.1, 0.5, 1.0, 7.0 and10.0 mg·L^{-1} working standards, where 0.00 mg·L^{-1} was acquired from a blank solution. After constructing the calibration curve with the R^2 of 0.998–0.999, the quality control check (QC) was evaluated by measuring the concentration of the blank and middle standard (1.0 mg·L^{-1}). The analysis was performed at the wavelength maxima of each metal ion measured. The analysis was performed at source equilibrium, nebulizer flow, auxiliary flow, plasma flow, pump rate, read delay of 15 s, 0.8 L·min^{-1}, 0.2 L·min^{-1}, 15 L·min^{-1}, 1.5 L·min^{-1}, where peak area was used as processing mode with at least 3 replicates.

On one hand, anions namely PO_4^{3+}, SO_4^{2+}, NO_3^-, Cl^-, F^- were analysed using ion chromatography (Eco IC, Metrohm) equipped with Metrosep A Supp 17-150/4.0 column and MagIC Net software. A mixed standard containing the above-mentioned anions was used as a stock solution to prepare a series of 0.5, 1.0, 5.0, 10, 50 and 100 mg·L^{-1} working standards. The analysis was performed under flow rate and recording time of 1.0 mL·min^{-1} and 13 min respectively. The buffer solution of 5 mM Na_2CO_3 and 16 mM $NaHCO_3$ was used as eluent while 0.1 M H_3PO_4 was used as a suppressing solution. The samples concentrations were acquired from the constructed calibration plots whose correlation coefficient was 0.99 for all analytes.

Membrane crystallization tests

Prior to membrane distillation crystallization (MDCr), the samples were filtered through a sand packed column with packing density of approximately 1.45–1.50 g·cm^{-3}, achieving the gravity-driven flow rate of ~0.21 L·h^{-1}. A lab-assembled module consisting of 21 hollow fibre polypropylene (PP) membranes (42 cm length, 0.2 µm pore size, 1.8 mm inner diameter, 450 µm thickness and 73% porosity) was used in MDCr processing of pretreated AMD feed water. The PP membrane was selected based on its hydrophobicity, affordability and commercial availability. This membrane offered a balance trade-off between chemical resistance and mechanical stability, making it suitable for AMD treatment in MDCr[62]. Although polytetrafluoroethylene (PTFE) and polyvinylidene (PVDF) have superior chemical resistance, they are costly and often require additional modifications to improve performance[63]. Also, PP exhibit low thermal conductivity and favourable pore structure which maintain stable temperature gradient and improve vapour permeability while exclusively

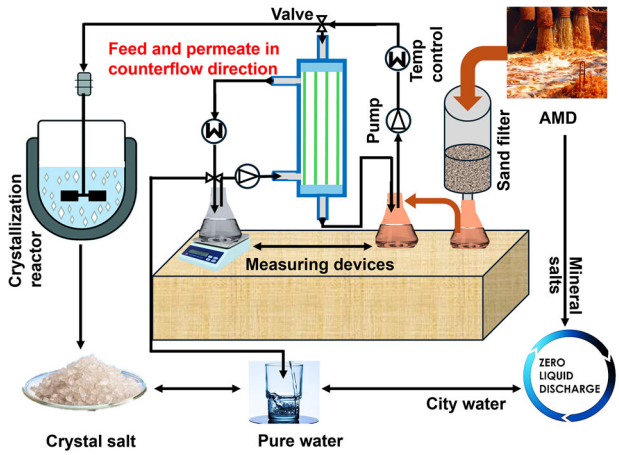

Fig. 7 | Schematic illustration of the MDCr systems used for recovery of freshwater and mineral salts from the AMD of a closed mine.

retaining non-volatile compounds[64]. Given the objective of this study involving treatment of AMD while maintaining cost-effectiveness for potential large-scale applications, the choice of PP membrane was inevitable.

The MDCr experimental sept-up was designed using a direct contact hollow fibre PP membrane module (Fig. 7). The feed and permeate solutions were driven by MasterFlex L/S peristaltic pump at a crossflow velocity of 14.03 mL/sec in a counter current configuration, following a previously reported method[30]. The permeate temperature was maintained at 10 °C with recirculating chiller while feed temperatures were varied between 50, 60 and 70 °C using PID-controlled water bath. The actual temperature of the feed and permeate were measured at module inlet and outlet. These measurements facilitated determination of the temperature difference stability across the two interfaces of the membrane using Eqs. 1–3. The water flux and salt rejection were calculated from Eqs. 4 and 5 using the measured permeate weight and conductivity from weighing balance (Adam Equipment LBX 3) and Hanna HI-5522-02 Professional bench top pH/ISE/EC dual channel meter respectively. Similarly, the conductivity of the feed solution was monitored to understand saturation and crystal formation. The pH of the feed and permeate were monitored using bench top pH/ISE/EC dual channel meter. All measurements were recorded at 5 min intervals except real-time monitoring of crystallization which was measured at 20 min intervals. The supersaturated solution with more than 80% water recovery was transferred to an external jacketed borosilicate glass crystallization reactor equipped with mechanical stirrer. The crystallization process was controlled under 150 mbar to improve solvent evaporation, stirring speed of 150 rpm for uniform saturation, and jacket temperature of 25 °C.

$$\Delta T_{In} = \frac{\Delta T_{in} - \Delta T_{out}}{In \frac{\Delta T_{in}}{\Delta T_{out}}} \quad (1)$$

$$\Delta T_{in} = T_{feed,in} - T_{permeate,out} \quad (2)$$

$$\Delta T_{out} = T_{feed,out} - T_{permeate,in} \quad (3)$$

$$J = \frac{dm}{Adt} \quad (4)$$

$$R(\%) = \frac{k_f - k_p}{k_f} x100\% \quad (5)$$

Where J, $R(\%)$, dm, A, dt, k_f and k_p represent water flux, percentage salt rejection, mass difference at time (t), change in time, feed and permeate conductivity respectively.

Crystal characterization

The supersaturated feed samples were collected at 20-min interval to monitor crystal formation and growth under optical microscope. ImageJ software was used to measure the particles from the obtained microscopic images. To ensure a true reflection of particle size distribution, a minimum of 100 crystals was analysed. The crystal particle growth rate was calculated from a linearized plot of particle size as a function of time[30,65], taking into account the effective growth rate as the time derivative of the crystal size. Equation 6 was linearized to Eq. 7 where the change in crystal length was plotted against growth time and the slope of the curve was used to calculate the crystal growth rate (G^{eff})[30].

$$G^{eff} = \frac{1}{2}\frac{dL}{dt} \quad (6)$$

$$dL = 2G^{eff}dt \quad (7)$$

Where dL, dt, and G^{eff} were change in crystal length, growth time and effective growth rate. Constant factor ($\frac{1}{2}$) accounts for particle growth from crystal centre to two opposite directions.

The mineral phase of the recovered crystals was identified using Bruker D2 Phaser Powder X-ray diffractometer equipped with a Cu Kα X-ray source (1.54 nm). The elemental analysis of the dried crystals was conducted using ICP-OES and IC analysis. Prior to analysis, 0.01 g of the crystal salts was dissolved in 1.0 L of deionized water, acidified with 0.1 M HNO_3 (1 mL) and digested for 60 min using the multiwave 5000 microwave reaction system. The final concentration of ions per recovered mass from MDCr system was calculated using Eq. 8.

$$C_{ion,MDC} = \frac{C_{ion,measured} * m_{MDC}}{m_{measured}} \quad (8)$$

Where $C_{ion,MDCr}$ and m_{MDCr} are the concentration and mass of ions per mass of crystal salts collected from the MDCr systems while $C_{ion,measured}$ and $m_{measured}$ are the concentration and mass of ions per used mass (0.01 g) during ICP-OES and IC analysis. All instruments were calibrated with certified standards.

Data availability

The authors declare that the data supporting the current findings of this study is available within the manuscript. Should any raw data be required, please contact the corresponding author.

Code availability

There is no available code. Please contact the corresponding author to access the detailed information.

Received: 10 April 2025; Accepted: 7 June 2025;
Published online: 05 July 2025

References

1. Knoche, S. & Ritchie, K. A travel cost recreation demand model examining the economic benefits of acid mine drainage remediation to trout anglers. *J. Environ. Manag.* **319**, 115485 (2022).
2. Smith, J., Sheridan, C., van Dyk, L. & Harding, K. G. Critical evaluation of the chemical composition of acid mine drainage for the development of statistical correlations linking electrical conductivity with acid mine drainage concentrations. *Environ. Adv.* **8**, 100241 (2022).
3. Oberholster, P. J. et al. An ecotoxicological screening tool to prioritise acid mine drainage impacted streams for future restoration. *Environ. Pollut.* **176**, 244–253 (2013).
4. Masindi, V. et al. Challenges and avenues for acid mine drainage treatment, beneficiation, and valorisation in circular economy: A review. *Ecol. Eng.* **183**, 106740 (2022).

5. Davies, T. C. & Mundalamo, H. R. Environmental health impacts of dispersed mineralisation in South Africa. *J. Afr. Earth Sci.* **58**, 652–666 (2010).
6. Moyé, J. et al. Groundwater assessment and environmental impact in the abandoned mine of Kettara (Morocco). *Environ. Pollut.* **231**, 899–907 (2017).
7. Kodirov, O., Kersten, M., Shukurov, N. & Martín Peinado, F. J. Trace metal(loid) mobility in waste deposits and soils around Chadak mining area, Uzbekistan. *Sci. Total Environ*. 1658–1667, (2018),
8. Department of Water Affairs and Forestry. Vol. 1: Domestic Water Use. in *South African Water Quality Guidelines* (Pretoria, 1996).
9. Republic of South Africa. National Water Act. *Gov. Gaz*. **Act No**. **36**, (1998).
10. Hou, D. et al. Simultaneous removal of iron and manganese from acid mine drainage by acclimated bacteria. *J. Hazard. Mater.* **396**, 122631 (2020).
11. Abiye, T. A. & Ali, K. A. Potential role of acid mine drainage management towards achieving sustainable development in the Johannesburg region, South Africa. *Groundw. Sustain. Dev.* **19**, 100839 (2022).
12. Munyengabe, A., Zvinowanda, C., Zvimba, J. N. & Ramontja, J. Innovative oxidation and kinetic studies of ferrous ion by sodium ferrate (VI) and simultaneous removal of metals from a synthetic acid mine drainage. *Phys. Chem. Earth* **124**, 102932 (2021).
13. Sithole, N. T., Ntuli, F. & Okonta, F. Synthesis and evaluation of basic oxygen furnace slag based geopolymers for removal of metals and sulphates from acidic industrial effluent-column study. *J. Water Process Eng.* **37**, 101518 (2020).
14. Ighalo, J. O. et al. A review of treatment technologies for the mitigation of the toxic environmental effects of acid mine drainage (AMD). *Process Saf. Environ. Prot.* **157**, 37–58 (2022).
15. Werner, A. et al. Nanofiltration for the recovery of indium and germanium from bioleaching solutions. *Sep. Purif. Technol.* **224**, 543–552 (2019).
16. Goyburo-Chávez, C. et al. Pilot-scale reverse osmosis treatment of gold cyanidation effluent for the removal of cyanide, heavy metal(loid) s, and ionic species. *Case Stud. Chem. Environ. Eng.* **9**, 100688 (2024).
17. Gusti Wibowo, Y., Safitri, H. et al. Recent advances in acid mine drainage treatment through hybrid technology: Comprehensive review of scientific literature. *Environ. Nanotechnol., Monit. Manag.* **21**, 100945 (2024).
18. Mahlangu, O. T. et al. The impact of nanoparticle leach on sustainable performance of the membranes – A critical review. *Environ. Nanotechnol., Monit. Manag.* **22**, 100984 (2024).
19. Yousry, A. et al. Performance model for reverse osmosis. *Chem. Eng. Res. Des.* **186**, 416–432 (2022).
20. Nthunya, L. N. et al. Progress in membrane distillation processes for dye wastewater treatment: A review. *Chemosphere* **360**, 142347 (2024).
21. Shi, W. et al. Construction of rough and porous surface of hydrophobic PTFE powder-embedded PVDF hollow fiber composite membrane for accelerated water mass transfer of membrane distillation. *J. Ind. Eng. Chem.* **108**, 328–343 (2022).
22. Nthunya, L. N. et al. Fouling, performance and cost analysis of membrane-based water desalination technologies: A critical review. *J. Environ. Manag.* **301**, 113922 (2022).
23. Zou, T., Kang, G., Zhou, M., Li, M. & Cao, Y. Investigation of flux attenuation and crystallization behavior in submerged vacuum membrane distillation (SVMD) for SWRO brine concentration. *Chem. Eng. Process. - Process. Intensif.* **143**, 107567 (2019).
24. Drioli, E., Ali, A. & Macedonio, F. Membrane distillation: Recent developments and perspectives. *Desalination* **356**, 56–84 (2015).
25. Nthunya, L. N., Setati, B., Richards, H., Chimuka, L. & Mamba, B. B. From extract to crystals: Unlocking green nanotechnology towards recovery of bioactive compounds from Moringa oleifera via membrane distillation crystallization. *Sep. Purif. Technol.* **373**, 133552 (2025).
26. Kavitha, E. et al. Current status and future prospects of membrane separation processes for value recovery from wastewater. *Chemosphere* **291**, 132690 (2022).
27. Candeias, C. et al. Acid mine drainage from the Panasqueira mine and its influence on Zêzere river (Central Portugal). *J. Afr. Earth Sci.* **99**, 705–712 (2014).
28. Yilmaz, T. et al. Treatment of acidic mine drainage in up-flow sulfidogenic reactor: Metal recovery and the pH neutralization. *J. Water Process Eng.* **32**, 100916 (2019).
29. Jiang, X., Niu, Y., Du, S. & He, G. Membrane crystallization: Engineering the crystallization via microscale interfacial technology. *Chem. Eng. Res. Des.* **178**, 454–465 (2022).
30. Nthunya, L. N., Pinier, J., Ali, A., Quist-jensen, C. & Richards, H. Valorization of acid mine drainage into potable water and valuable minerals through membrane distillation crystallization. *Sep. Purif. Technol.* **334**, 126084 (2024).
31. Asif, M. B. et al. Acid mine drainage and sewage impacted groundwater treatment by membrane distillation: Organic micropollutant and metal removal and membrane fouling. *J. Environ. Manag.* **291**, 112708 (2021).
32. Riekert, S. M., Winston, R. J. & Burris, L. E. Pervious concrete for treatment of acid mine drainage: Neutralization of pH and removal of dissolved iron, aluminum, manganese, and copper. *J. Environ. Manag.* **375**, 124188 (2025).
33. Yan, Z. et al. Effect of biopolymers and humic substances on gypsum scaling and membrane wetting during membrane distillation. *J. Memb. Sci.* **617**, 118638 (2021).
34. Flatscher, S., Hell, F., Hlawitschka, M. W. & Lahnsteiner, J. Seeded membrane distillation crystallization for hypersaline brine treatment. *Water Reuse* **14**, 16–29 (2024).
35. Julian, H. et al. Numerical study of CaCO3 scaling in submerged vacuum membrane distillation and crystallization (VMDC). *J. Memb. Sci.* **559**, 87–97 (2018).
36. Udhayakumar, R., Manivannan, P., Raghu, K. & Vaideki, S. Assessment of physico-chemical characteristics of water in Tamilnadu. *Ecotoxicol. Environ. Saf.* **134**, 474–477 (2016).
37. Chrysochoou, M., Dermatas, D. & Grubb, D. G. Phosphate application to firing range soils for Pb immobilization: The unclear role of phosphate. *J. Hazard. Mater.* **144**, 1–14 (2007).
38. Charfi, A., Tibi, F., Kim, J., Hur, J. & Cho, J. Organic fouling impact in a direct contact membrane distillation system treating wastewater: Experimental observations and modeling approach. *Membr. (Basel)* **11**, 493 (2021).
39. Quist-Jensen, C. A., Ali, A., Mondal, S., Macedonio, F. & Drioli, E. A study of membrane distillation and crystallization for lithium recovery from high-concentrated aqueous solutions. *J. Memb. Sci.* **505**, 167–173 (2016).
40. Dudchenko, A. V. et al. Impact of module design on heat transfer in membrane distillation. *J. Memb. Sci.* **601**, 117898 (2020).
41. Fontananova, E. et al. Turning mine-tailing streams into sources of water and mineral salts in a membrane-sustained circular scenario. *npj Clean. Water* **7**, 112 (2024).
42. Skuse, C., Gallego-Schmid, A., Azapagic, A. & Gorgojo, P. Can emerging membrane-based desalination technologies replace reverse osmosis?. *Desalination* **500**, 114844 (2021).
43. Silva, M. R., Reis, B. G., Grossi, L. B. & Amaral, M. C. S. Improving the energetic efficiency of direct-contact membrane distillation in mining effluent by using the waste-heat-and-water process as the cooling fluid. *J. Clean. Prod.* **260**, 121035 (2020).
44. Liu, Y., Sun, Y. & Peng, Z. Evaluation of bipolar membrane electrodialysis for desalination of simulated salicylic acid wastewater. *Desalination* **537**, 115866 (2022).

45. Li, X., Qin, Y., Liu, R., Zhang, Y. & Yao, K. Study on concentration of aqueous sulfuric acid solution by multiple-effect membrane distillation. *Desalination* **307**, 34–41 (2012).
46. Koo, C. H., Mohammad, A. W., Suja', F. & Meor Talib, M. Z. Review of the effect of selected physicochemical factors on membrane fouling propensity based on fouling indices. *Desalination* **287**, 167–177 (2012).
47. Aligwe, P. A., Sirkar, K. K., Canlas, C. J. & Cheng, W. C. Supported gas membrane-based ammonia removal and recovery for a pH-dependent sink: Effect of water vapor transport. *J. Memb. Sci.* **611**, 118308 (2020).
48. Fu, H., Li, M., Huang, J. & Cao, S. Insights into the Role of Na+ on the Transformation of Gypsum into α-Hemihydrate Whiskers in Alcohol–Water Systems. *ACS Omega* **7**, 15570–15579 (2022).
49. Zheng, Y. Nonisothermal Crystallization Kinetics of Sodium Sulfate Produced by Stirred Crystallization. *Russ. J. Phys. Chem. A* **97**, 3227–3237 (2023).
50. Yadav, A., Labhasetwar, P. K. & Shahi, V. K. Membrane distillation crystallization technology for zero liquid discharge and resource recovery: Opportunities, challenges and futuristic perspectives. *Sci. Total Environ.* **806**, 150692 (2022).
51. Mapetere, A., Di Profio, G., Curcio, E., Campo, P. & McAdam, E. J. Unifying nucleation and crystal growth mechanisms in membrane crystallisation. *J. Memb. Sci.* **725**, 124021 (2025).
52. Zi, G., Huang, B., Wen, Z., Li, W. & Luo, L. Nucleation thermodynamics and nucleation kinetics of (NH4)2SO4 under the action of NH4Cl. *J. Mol. Liq.* **377**, 121514 (2023).
53. Hong, B. et al. Controlling nucleation during unseeded THM growth of CdZnTe crystal. *J. Cryst. Growth* **534**, 125482 (2020).
54. Ding, S. S. et al. Morphology evolution of barium oxalate hydrate controlled by poly (sodium-4-styrenesulfonate). *Powder Technol.* **249**, 140–145 (2013).
55. Teychené, S., Rodríguez-Ruiz, I. & Ramamoorthy, R. K. Reactive crystallization: From mixing to control of kinetics by additives. *Curr. Opin. Colloid Interface Sci.* **46**, 1–19 (2020).
56. Grigg, A. R. C., Notini, L., Kaegi, R., ThomasArrigo, L. K. & Kretzschmar, R. Structural Effects of Aluminum and Iron Occupancy in Minerals of the Jarosite-Alunite Solid Solution. *ACS Earth Sp. Chem.* **8**, 194–206 (2024).
57. Seyed Sabour, S. M. J. & Ghorashi, B. A comprehensive review of major water desalination techniques and mineral extraction from saline water. *Sep. Purif. Technol.* **349**, 127913 (2024).
58. Feng, H. et al. Recent progress in melt crystallization. *Chem. Eng. Res. Des.* **190**, 268–281 (2023).
59. Wantha, L. & Flood, A. E. Crystal growth rates and secondary nucleation threshold for γ-dl-methionine in aqueous solution. *J. Cryst. Growth* **318**, 117–121 (2011).
60. Demers, I. et al. Use of acid mine drainage treatment sludge by combination with a natural soil as an oxygen barrier cover for mine waste reclamation: Laboratory column tests and intermediate scale field tests. *Miner. Eng.* **107**, 43–52 (2017).
61. Jafaripour, A., Rowson, N. A. & Ghataora, G. S. Utilisation of residue gas sludge (BOS sludge) for removal of heavy metals from acid mine drainage (AMD). *Int. J. Miner. Process.* **144**, 90–96 (2015).
62. Saleem, J., Moghal, Z. K. B. & McKay, G. Harnessing plastic waste for sustainable membrane filtration with trimodal structure through acid-catalyzed oxidation. *Chem. Eng. J.* **486**, 150230 (2024).
63. Turk, O. K., Zoungrana, A. & Cakmakci, M. Performances of PTFE and PVDF membranes in achieving the discharge limit of mixed anodic oxidation coating wastewaters treated by membrane distillation. *Environ. Sci. Pollut. Res* **31**, 39663–39677 (2024).
64. Hossain, M. T. et al. Research and application of polypropylene: a review. *Discov. Nano* **19**, 2 (2024).
65. Spillar, V. & Dolejs, D. Calculation of Time-dependent Nucleation and Growth Rates from Quantitative T extural Data: Inversion of Crystal Size Distribution. *J. Petrol.* **54**, 913–931 (2013).

Acknowledgements

This research was funded by the Ministry of Foreign Affairs of Denmark (MFA) through the Danida Fellowship Centre (DFC), project no. 20-M01AAU, "Membrane crystallization for water and mineral recovery" and National Research Foundation (grant numbers: CSRP23042496727 and PSTD240424215871). The study was conducted at University of the Witwatersrand and University of South Africa, in collaboration with Aalborg University (Denmark). Support from NRF, MFA and these universities is highly acknowledged.

Author contributions

L.N.N.: Conceptualization, Methodology, Data curation, Software, Writing-Original draft preparation, Reviewing and Editing, A.A.: Data curation, Writing- Original draft preparation, Reviewing and Editing, HR: Conceptualization, Methodology, Data curation, C.Q.-J.: Conceptualization, Methodology, Data curation, Software. L.C.: Resources, Reviewing and Editing, B.B.M.: Supervision, Resources, Reviewing and Editing.

Competing interests

Professor Bhekie B. Mamba is the member of npj Clean Water editorial board, but he was not involved in the peer-review or decision-making process of this manuscript. Other authors declare that they have no known competing financial interests or personal relationships that could have appeared to influence the work reported in this paper.

Additional information

Correspondence and requests for materials should be addressed to Lebea N. Nthunya.